AIAA JOURNAL
Vol. 36, No. 5, May 1998

Unsteady Flowfield and Noise Propagation due to Transonic Airfoil–Airfoil Interaction

Kwanjung Yee,* Dong-Ho Lee,† and Soogab Lee‡
Seoul National University, Seoul 151-742, Republic of Korea

As a two-dimensional approximation to the outer region of a coaxial rotor, the flowfields induced by transonic airfoil–airfoil interaction are numerically simulated to investigate the aerodynamic and acoustic characteristics. The processes of aerodynamic load fluctuation are monitored with time for a transonic flowfield. It is observed that abrupt pressure disturbances around the leading edge of the upper airfoil induced by the shock wave of the lower airfoil and the ensuing oscillation of the shock wave cause the severe aerodynamic load fluctuation in the upper airfoil, and a strong sound wave is radiated from the upper airfoil in some cases. A series of parametric studies shows that both the intensity and the slope of the load fluctuation are more sensitive to vertical miss distance than to angle of attack, but the hysteresis in lift is more dependent on angle of attack. A modified approach is suggested to minimize the numerical compression wave generated when imposing an initial condition for an asymmetric unsteady flowfield, and it is shown to be very efficient for shortening the initial start distance, thereby saving computation time.

Nomenclature

C	= chord length
Cl_o	= initial lift coefficient
k	= reduced frequency, Strouhal number, $\omega C/2M_\infty$
M_l	= Mach number of lower airfoil moving left to right
M_u	= Mach number of upper airfoil moving right to left
M_∞	= freestream Mach number
Re	= Reynolds number
X_{miss}	= horizontal miss distance between the leading edges
Y_{miss}	= vertical miss distance between the leading edges
α_l	= angle of attack of lower airfoil
α_m	= amplitude of unsteady angle of attack in oscillating airfoil
α_o	= mean angle of attack in oscillating airfoil
α_u	= angle of attack of upper airfoil
ΔCl	= difference between minimum and initial lift coefficients
ΔCl_i	= lift coefficient difference from the initial value
$\Delta Cl_{\max}$	= difference between maximum and minimum lift coefficients

Introduction

THE aerodynamic interaction between moving bodies is one of the most challenging problems in computational fluid dynamics. There seem to be two major difficulties in handling such problems. One arises from the fact that it is difficult to impose an appropriate initial condition when the bodies move in opposite directions with respect to a stationary flowfield. The other results from the fact that enormous computation time is required to guarantee a reliable solution. However, with the rapid advances in computing capacity, newly developed methods[1–3] have made it possible to predict the properties of aerodynamic interaction such as store separation[4] and flap oscillation.[5,6] But few studies have been carried out on a multicomponent moving problem such as trains passing in a tunnel[7,8] and a counter-rotating propeller. The unsteady flowfields induced by two lifting bodies can be found in coaxial or tandem rotors. The coaxial rotor is notorious for its bad noise characteristics, and its aerodynamics are very complicated. But the detailed processes of aerodynamic interaction and the resulting load fluctuation are not fully understood yet.[9] Experimental research up to now has concentrated on the performance analysis dealing with the averaged values and has failed to investigate the unsteady aerodynamic and aeroacoustic processes.[10] As for the numerical approach, only a simple analysis using the local momentum theory is available because of the huge computing capacity and complicated vortex modeling.[11] The present study models the outboard section of the counter-rotating blades in a coaxial rotor and the overlap region of tandem rotors as the two airfoils passing each other. This approximation uses an argument very similar to that in the two-dimensional blade–vortex interaction,[12,13] and the resulting flowfield is named airfoil–airfoil interaction (AAI),[14] as shown in Fig. 1. The objectives of the present study are as follows: 1) understanding the detailed mechanism of aerodynamic interactions between the two airfoils, including viscous effects; 2) investigating the effects of vertical miss distance and angle of attack on the aerodynamic load fluctuation; 3) elucidating the major mechanism of noise propagation due to transonic AAI; and 4) suggesting a modified procedure of imposing an efficient initial condition that can be applied to the asymmetric unsteady flowfield. To handle a multicomponent moving configuration, a grid-embedding method called Chimera is employed, and a patched-grid method is also introduced for efficient grid distribution.

Numerical Method

Governing Equations and Numerical Schemes

Any flow would be most accurately modeled by the full Navier–Stokes equations. Even though most of the physics and important features of the flow can be captured with good accuracy using the Euler equations, Navier–Stokes equations must be used in the region where viscous effects are not negligible, as in shock–boundary interaction. The governing equations are the two-dimensional compressible Navier–Stokes equations written in the generalized coordinate system

$$\frac{1}{J}\frac{\partial \hat{Q}}{\partial t}+\frac{\partial \hat{E}}{\partial \xi}+\frac{\partial \hat{F}}{\partial \eta}=\frac{1}{Re}\left(\frac{\partial \hat{E}_v}{\partial \xi}+\frac{\partial \hat{F}_v}{\partial \eta}\right) \tag{1}$$

Because we are dealing with air, the equation of state for an ideal gas may be employed:

$$e=\frac{p}{\rho(\gamma-1)}+\frac{1}{2}(u^2+v^2) \tag{2}$$

The convective terms are discretized using Roe's flux difference splitting.[15] The primitive-variable extrapolation of the MUSCL[16,17] approach is employed for higher-order spatial accuracy. To take the turbulence effect into account, a simple algebraic Baldwin–Lomax

Received Jan. 14, 1997; revision received Dec. 5, 1997; accepted for publication Jan. 4, 1998.

*Graduate Research Assistant, Department of Aerospace Engineering. Member AIAA.
†Professor, Department of Aerospace Engineering. Senior Member AIAA.
‡Assistant Professor, Department of Aerospace Engineering. Senior Member AIAA.

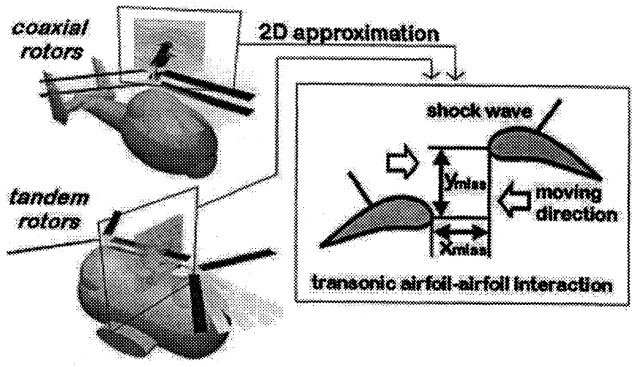

Fig. 1 Schematic of transonic AAI.

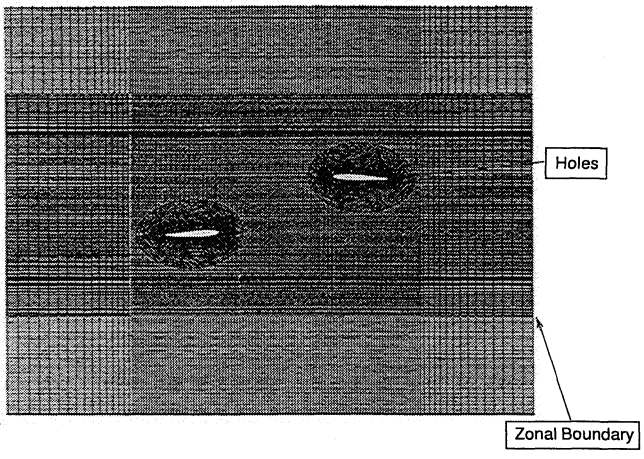

Fig. 2 Overset and patched-grid system for AAI configuration.

model[18] is used in the present study. An implicit approximate-factorization finite volume scheme for the two-dimensional equation[19] can be written as

$$\left[\frac{I}{J}+\Delta t\left(\delta_\xi^-\frac{\partial\hat{E}^+}{\partial Q}+\delta_\xi^+\frac{\partial\hat{E}^-}{\partial Q}\right)\right]^n \times\left[\frac{I}{J}+\Delta t\left(\delta_\eta^-\frac{\partial\hat{F}^+}{\partial Q}+\delta_\eta^+\frac{\partial\hat{F}^-}{\partial Q}\right)\right]^n=-\Delta t\hat{R} \tag{3}$$

Unfortunately, AF-ADI (Approximate Factorization-Alternating Direction Implicit) has only first-order temporal accuracy; Newtonian subiterations are used to restore the temporal order of accuracy to second order as well as to remove the linearization and factorization errors, thereby increasing the spatial accuracy as well.

Grid Generation

The advantage of the overlapping grid method lies in the free choice of grid type. Each grid must have sufficient resolution and satisfy orthogonality and smoothness to obtain a high-quality solution. The base flow is divided into five zones, and the resultant grid system is shown in Fig. 2. The larger H-type grid around the two airfoils that covers the entire flowfield is called the background grid. The smaller grids around the airfoils are submerged into the background grid and obtained by the hyperbolic grid generator. The patched-grid method is also introduced to use the limited number of grids with efficiency.[20] Because the middle region is of primary interest, a denser grid is used, whereas relatively coarser grids are used in the upper and lower background region. About 10^5 grid points are used to construct the entire flowfield.

Initial and Boundary Conditions

In periodic unsteady problems such as an oscillating airfoil, the imposition of an initial condition is very simple because the periodicity can be obtained within two or three cycles. However, it becomes a serious problem in the nonperiodic unsteady problems

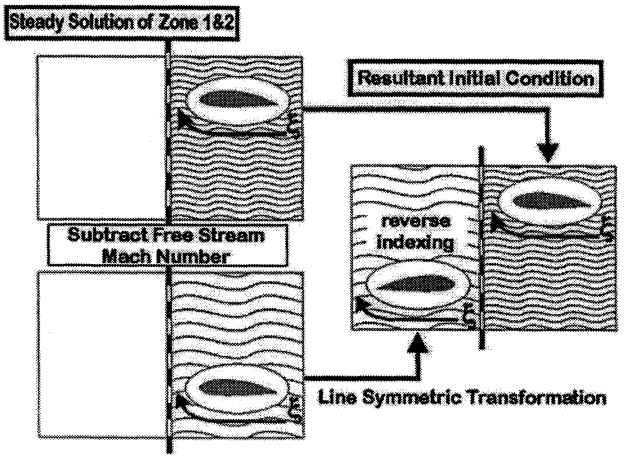

Fig. 3 New approach imposing asymmetric unsteady initial condition.

because unphysical compression waves may occur at the initial stage and deteriorate the final solution. Therefore, the bodies should be placed far away from each other in the beginning to avoid such a difficulty. In that case, it would require enormous computational time for the bodies to travel over the region of no interest. Hence, an appropriate initial condition that can avoid a compression wave is the key point to reduce overall computation time. In the analysis of a high-speed train moving into a tunnel, Ogawa and Fujii[7] suggested a procedure of imposing an initial condition that can avoid the unnecessarily long initial distance. The steady-state flow around the body in an unbounded flowfield is preliminarily obtained and is used as the initial condition. But a slight oscillation in the solution is observed, resulting from the interpolation between the disturbed train zone and the undisturbed background zone. The present study extends Ogawa and Fujii's idea to the flowfield where the two bodies move in opposite directions. A modified procedure has been introduced. 1) The steady-state solutions covering the entire flowfield are preliminarily obtained for each airfoil. 2) The freestream velocity is then subtracted from each of the steady solutions

$$\rho_o=\rho_s,\qquad u_o=u_s-u_\infty,\qquad v_o=v_s-v_\infty,\qquad p_o=p_s \tag{4}$$

$$e=\frac{p_o}{\rho(\gamma-1)}+\frac{1}{2}\left(u_o^2+v_o^2\right)$$

where u_s is the steady-state solution, u_∞ the freestream value, and u_o the value used in the initial start. 3) The primitive variables obtained from step 2 are imposed on respective halves. 4) For the left half of the flowfield they must be imposed in the line-symmetric way with respect to the centerline. 5) It is very important to note that reverse indexing is required for the airfoil zone placed in the left half so as to maintain the consistency of coordinate system. 6) Then the two airfoils start moving in the opposite direction:

$$(x_\tau)_l=u_\infty,\qquad (x_\tau)_u=-u_\infty \tag{5}$$

This procedure is depicted in FigA comparison is made with the original method suggested by Ogawa and Fujii[7] to verify the effectiveness of the present method. The flow has conditions with a Mach number of 0.8 and a vertical miss distance of $1.0C$. The angle of attack is 3 deg for both airfoils. Figure 4 shows the lift variation rate with different initial conditions. It is noticed that the present initial condition avoids strong compression waves created at the initial acceleration, whereas the other one shows a sudden decrease in lift from the beginning. As mentioned before, this error results from the interpolation between the undisturbed background flowfield and the airfoil region. This result indicates that the present method prevents numerical compression waves and yields reliable solutions even for a relatively short initial distance. The wall boundary condition is imposed on the airfoil surface. The nonreflecting boundary condition considering the one-dimensional propagation of characteristic variables is imposed at the far-field boundaries.

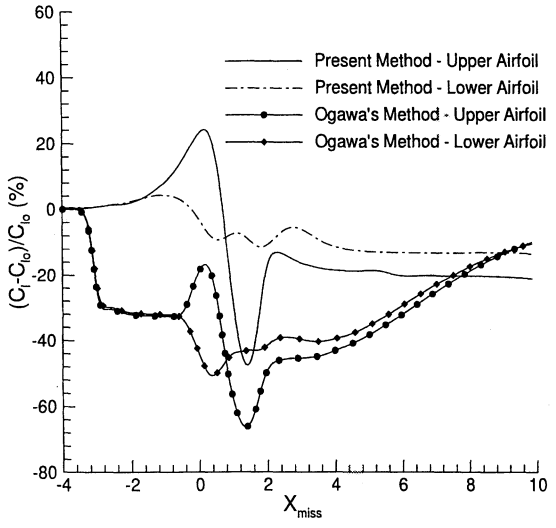

Fig. 4 Comparison of lift variation rate for different initial conditions ($M_l = 0.8$, $M_u = 0.8$, $\alpha_l = 3$ deg, $\alpha_u = 3$ deg, $Y_{miss} = 1.0C$, and $Re = 3 \times 10^6$).

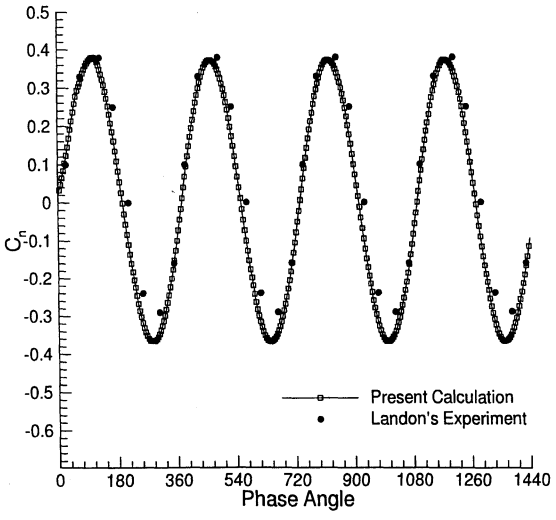

Fig. 5 Lift coefficient time history of a pitching NACA 0012 airfoil [$M_\infty = 0.755$, $\alpha_o = 0.016$ deg, $\alpha_m = 2.51$ deg, $k = 0.0814$, and $\alpha = \alpha_o + \alpha_m \sin(2M_\infty kt)$].

Results and Discussion

Validations: Oscillating Airfoil

To validate the accuracy of the present code, a numerical calculation is made for a NACA 0012 airfoil oscillating in pitch about its quarter-chord at a Mach number of 0.755 and a reduced frequency of 0.0814, where the reduced frequency, or Strouhal number, is defined as

$$k = (\omega C/2M_\infty) \tag{6}$$

The mean angle of attack α_o of the airfoil is 0.016 deg, and the unsteady angle-of-attack amplitude α_m is 2.51 deg. Then the angle of attack is given in nondimensional variables:

$$\alpha = \alpha_o + \alpha_m \sin(2M_\infty kt) \tag{7}$$

Experimental data are available for this case from Ref. 21, and a comparison of computed results with the experimental data is presented in Fig. 5. Airfoil motion is implemented by rotating the minor grid as a rigid body about the pitch axis. Figure 5 is a plot of the experimental vs the computed lift coefficient history. The calculation starts with initial conditions of freestream values everywhere and continues until the airfoil undergoes four cycles of pitching motion to allow unsteady transients to decay. The aerodynamic coefficients show a periodicity from the second period and agree well with the experimental results. Although a slight time lag is observed in the lift coefficient history, the present code is shown to be accurate enough to capture the location and unsteady motion of a shock.

Mechanism of Aerodynamic Load Fluctuation

To understand the aerodynamic mechanism during the interaction, a computation has been performed with the following flow conditions, and the results are monitored with respect to time. Both airfoils have 3-deg angles of attack and move with a velocity of $M = 0.8$; the Reynolds number based on the chord length is 3×10^6. The vertical miss distance Y_{miss} is $1.0C$. Figures 6a–6d show a series of pressure contours and coefficients at four different positions, and the pressure coefficient distributions at each location are compared with initial values. There is no remarkable change in the lift coefficient up to $X_{miss} = -0.75C$. At $X_{miss} = -0.75C$, the lowest pressure of the suction side of the upper airfoil slightly increases, and the location of the shock wave begins to move backward. At the same time, the intensity of the stagnation pressure is weakened from the interaction with the lower-pressure region of the lower airfoil. On the other hand, the lower airfoil shows the opposite behavior. This trend continues until $X_{miss} = 0.25C$. But no remarkable variation in the lift is observed until $X_{miss} = 0.75C$ in spite of the changes in the pressure distribution. This results from the fact that for the upper airfoil the loss of lift due to the reduction of stagnation pressure is compensated by the increase in the lowest pressure of the upper surface, whereas for the lower airfoil the loss of lift due to pressure increase of the upper surface is alleviated by the retardation of the shock wave location. At $X_{miss} = 0.75C$, the lift of the upper airfoil begins to decrease abruptly because the intensity of the stagnation pressure is suddenly weakened by the interaction with the suction side of the lower airfoil. At this location, the shock wave of the lower airfoil reaches around the leading edges of the upper airfoil, and the strong nose-down pitching moment is felt by the upper airfoil. The stagnation pressure of the upper airfoil is weakened to about -0.50, and the lift decreases continuously until $X_{miss} = 2.0C$. After that, the shock wave location of the upper airfoil moves upstream, whereas that of the lower airfoil goes downstream. The process is clearly shown in Fig. 6d, and this is why the fluctuation of the lift for the lower airfoil is kept relatively small during the AAI. In other words, the lift loss of the lower airfoil is partly compensated by the change in the shock location. When $X_{miss} = 3.0C$, the overall lift of the upper airfoil is recovered gradually as the stagnation pressure goes back to its initial level. Meanwhile, the shock wave of the lower airfoil retarded farther downstream, but it is not yet recovered to its original position. This trend continues by $X_{miss} = 8.0C$. But still there is a significant discrepancy in lifts between the two airfoils. This implies the existence of a hysteresis during the AAI. Hence it is expected that a longer distance is required for the airfoils to recover their original states. The physics of hysteresis will be discussed in the next section. In brief, the primary sources of aerodynamic load fluctuation may be due to the pressure fluctuation around the leading edge during the interaction, more precisely, the abrupt change in stagnation pressure and the transition of the shock wave position.

Hysteresis

To learn why the aerodynamic coefficients do not recover their original values after the two airfoils pass one another, Mach contours are depicted at two different angles of attack of the lower airfoil. In Fig. 7, the horizontal and vertical miss distances are $5.0C$ and $1.5C$, respectively. The angle of attack of the upper airfoil is kept at 10 deg, whereas that of the lower airfoil is 3 and 7 deg. As the airfoils travel in the computational domain, the wake regions are induced at the back of each airfoil, and their intensity increases proportional to the angle of attack. The wake remains quite long after the airfoils pass and influences the ambient flowfield, as shown in Fig. 7. Accordingly, the airfoils confront the flow condition that is different from the initial state. That is, the upper airfoil undergoes the downward velocity component, which is formed in the wake region of the lower airfoil. The downward velocity component decreases the effective angle of attack of the upper airfoil. Hence, as long as the airfoils travel in the wake region, the aerodynamic coefficients will not recover their original values. For the lower airfoil, the situation is contrary to that of the upper airfoil. The effective angle of attack of the lower airfoil increases by the upward velocity component, and the lift loss during the AAI is partly compensated. Because numerical dissipation is the only factor that attenuates the intensity of the wake in the inviscid

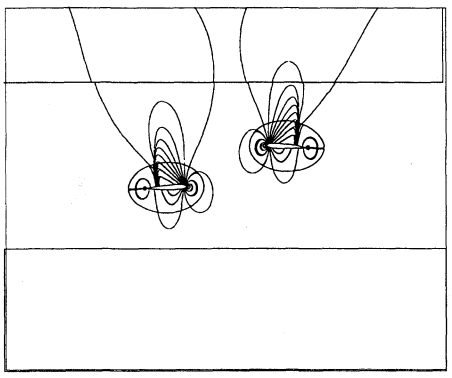
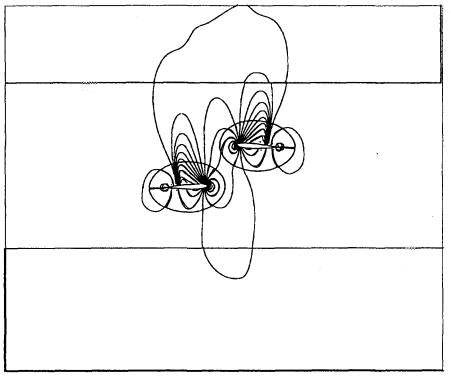
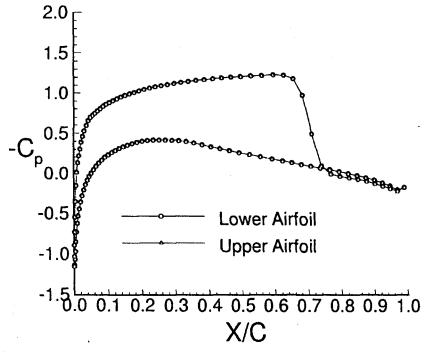

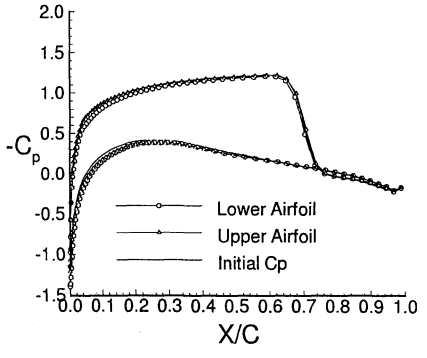

a) Pressure and C_p at $X_{\text{miss}} = -2.0C$

Pressure and C_p at $X_{\text{miss}} = -0.75C$

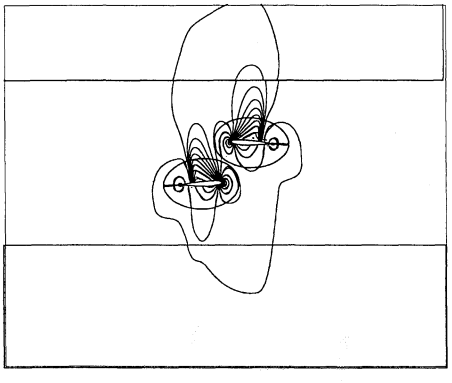
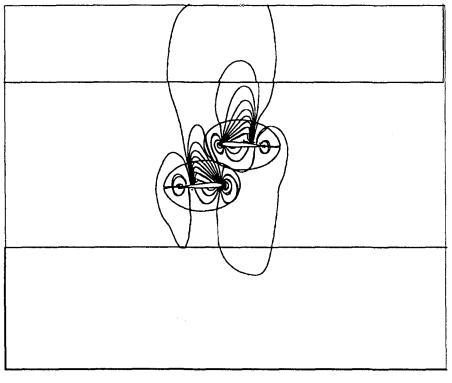
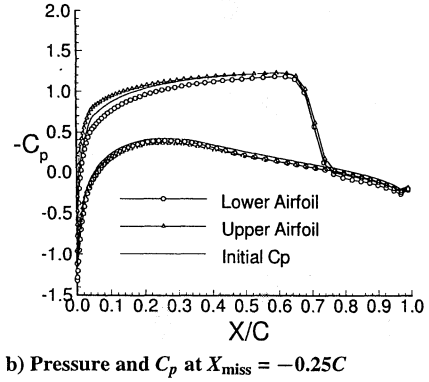

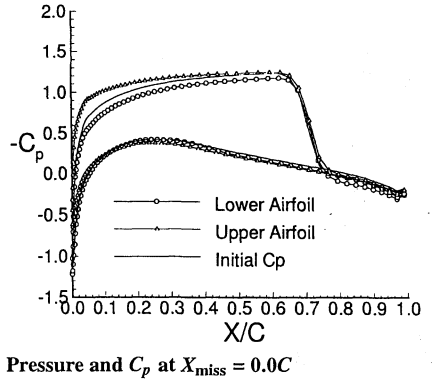

b) Pressure and C_p at $X_{\text{miss}} = -0.25C$

Pressure and C_p at $X_{\text{miss}} = 0.0C$

Fig. 6 Snapshots of C_p and pressure contours ($M_l = 0.8$, $M_u = 0.8$, $\alpha_l = 3$ deg, $\alpha_u = 3$ deg, $Y_{\text{miss}} = 1.0C$, and $Re = 3 \times 10^6$).

calculation, the influence of the wake will last longer in viscous calculation. As will be shown later, the strength of the hysteresis directly depends on the intensity of the angle of attack rather than on the vertical miss distance.

Propagation of the Sound Wave

In this section, the formation and propagation of a sound wave from the upper airfoil will be considered qualitatively rather than quantitatively. The sound wave is a propagating fluctuation in pressure, caused by an unsteady aerodynamic flowfield. It is well known that the intensity of the sound wave is related to the amplitude and time derivative of the fluctuating force around the airfoil. In compact source theory, the resulting pressure disturbance due to a fluctuating force is divided into two parts. One part is the reactive field, which dominates near the airfoil with an amplitude that is proportional to the fluctuating force. The other part, known as the radiation field, has an amplitude that is proportional to the time derivative of the fluctuating force. Although the reactive field dominates in the vicinity of

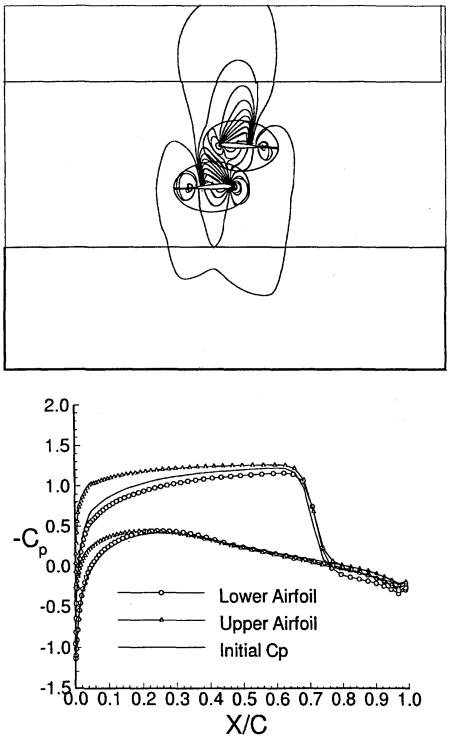

c) Pressure and C_p at $X_{miss} = 0.25C$

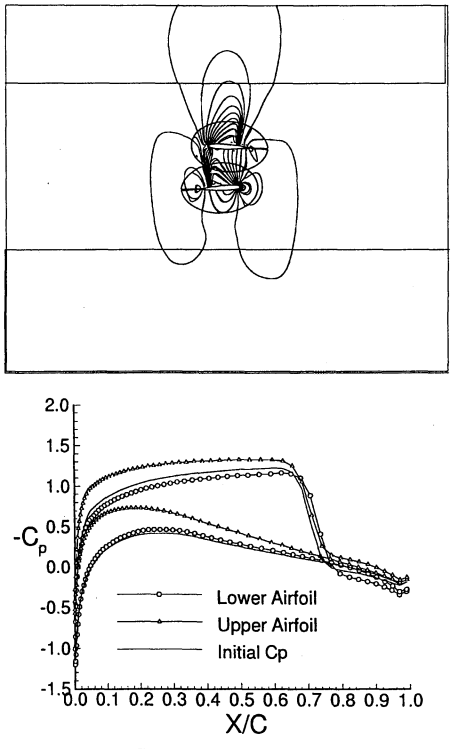

Pressure and C_p at $X_{miss} = 0.75C$

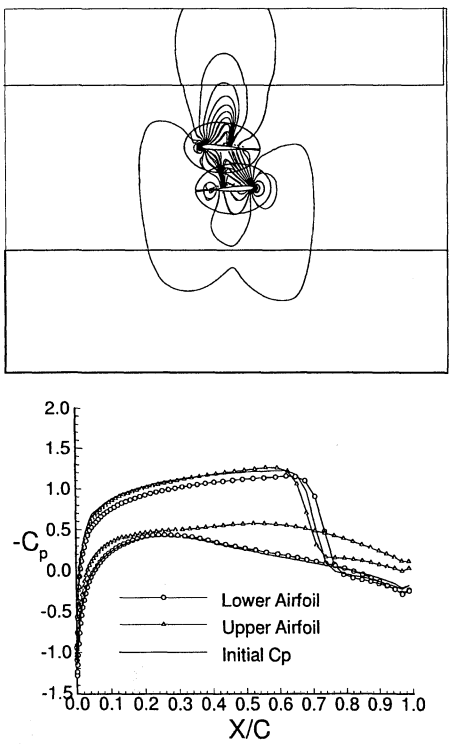

d) Pressure and C_p at $X_{miss} = 1.35C$

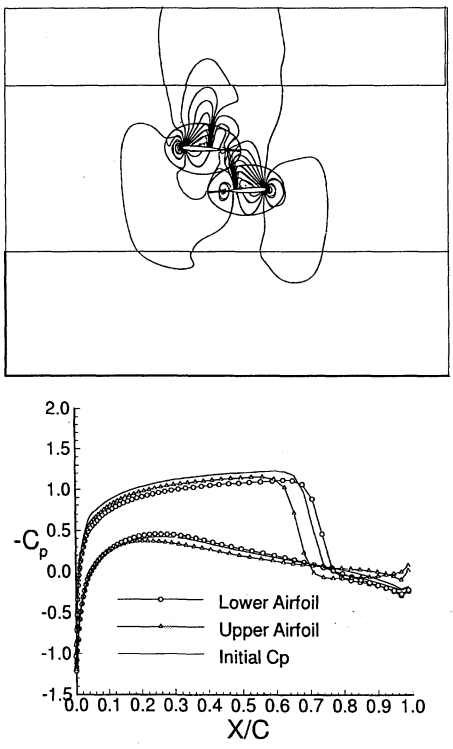

Pressure and C_p at $X_{miss} = 2.0C$

Fig. 6 Continued.

the airfoil, it is the radiation field that eventually propagates to the far field and forms the acoustic wave. The amplitude and the time derivative of the fluctuating force undergo great change during AAI. Hence, it is natural to expect that significant noise will be generated from the upper airfoil. Pressure histories of five observation points around the upper airfoil are shown in Fig. 8. From Fig. 8 and previous results, the formation of a sound wave is explained as follows. 1) The shock wave of the lower airfoil induces an abrupt pressure disturbance in the near field around the leading edge. 2) The fast oscillation of the shock wave follows. 3) A sound wave is generated from the upper airfoil and propagates downward. Four pressure contour plots are shown in Fig. 9 right after the lift variation reaches its maximum. It is clearly shown that the sound wave is generated and propagated downward from the upper airfoil. Although the acoustic phenomenon is essentially three dimensional, a two-dimensional acoustic analogy and its solution can be derived by integrating the three-dimensional equation along an infinite span.[22] The far-field acoustic perturbations around the upper airfoil are obtained from

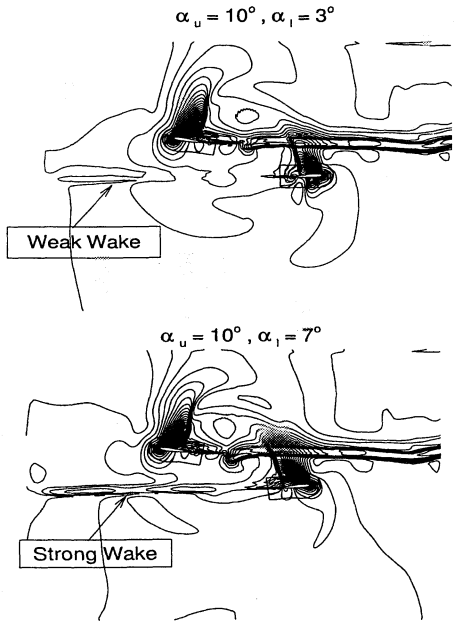

Fig. 7 Mach contours at two different lower airfoil angle-of-attack cases ($M_l = 0.8$, $M_u = 0.8$, $\alpha_l = 3$ and 7 deg, $\alpha_u = 10$ deg, $X_{miss} = 5.0C$, and $Y_{miss} = 1.5C$).

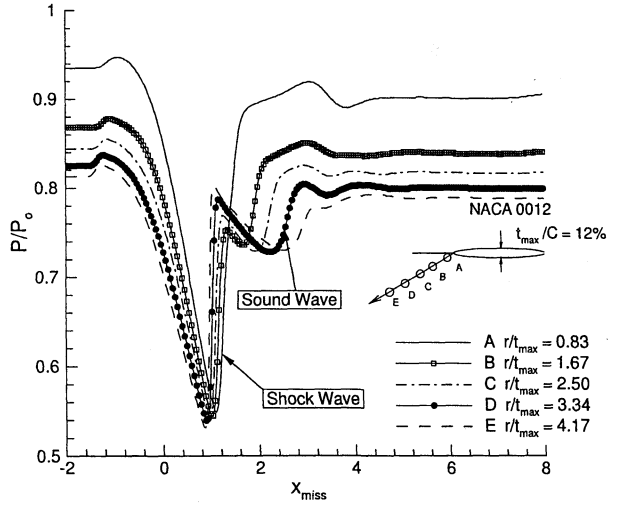

Fig. 8 Time histories of pressure at five observation points around the upper airfoil ($M_l = 0.8, M_u = 0.8, \alpha_l = 10$ deg, $\alpha_u = 10$ deg, $Y_{miss} = 1.0C$, and $Re = 3 \times 10^6$).

Curle's analysis, which incorporates the influence of solid boundaries upon the sound field.[23] The two-dimensional Curle equation for a far-field sound field from a compact source is described as follows;

$$\rho(\boldsymbol{x}, t) - 1 = \frac{M^3}{2\pi}\frac{x_i}{x}\int_0^\infty \frac{\partial}{\partial t^*}\int n_j p_{ij}(\boldsymbol{y}, t^*)\,\mathrm{d}\boldsymbol{y}\,\mathrm{d}\xi + \frac{M^4}{2\pi}\frac{x_i x_j}{x^2}\int_0^\infty \frac{\partial^2}{\partial t^{*2}}\int T_{ij}(\boldsymbol{y}, t^*)\,\mathrm{d}^2\boldsymbol{y}\,\mathrm{d}\xi \tag{8}$$

where

$$t^* = t - M|\boldsymbol{x}|\cosh\xi$$

$$p_{ij} = p\delta_{ij} - \tau_{ij}$$

$$\tau_{ij} = \frac{1}{Re}\left(\frac{\partial u_i}{\partial x_j} + \frac{\partial u_j}{\partial x_i}\right)$$

where $\boldsymbol{x}$ is the position vector of an observer and $\boldsymbol{y}$ the position vector of a noise source.

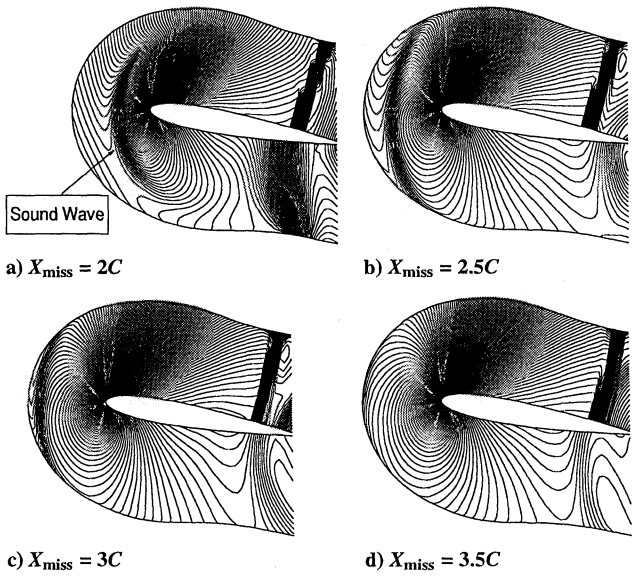

Fig. 9 Snapshots of pressure contours around upper airfoil ($M_l = 0.8$, $M_u = 0.8$, $\alpha_l = 10$ deg, $\alpha_u = 10$ deg, $Y_{miss} = 1.0C$, and $Re = 3 \times 10^6$).

Because the body of interest is in motion, the acoustic perturbations are calculated in terms of two coordinate systems. Figure 10a shows the acoustic density due to the sum of lift and drag dipole contributions with respect to the moving coordinate. Because there is no relative motion between the airfoil and the observer, lift dipole dominates the acoustic field, and the sound wave propagates along the vertical direction, namely the lift dipole axis. The acoustic density contour, which considers the relative motion, is depicted in Fig. 10b. It is shown that the sound wave propagates in the forward and downward direction due to Doppler effects. Now that the rapid transition of the surface pressure dominates the flowfield, it is expected that dipole characteristics will be the major noise source. As will be shown later, the strength of the aerodynamic fluctuation is very sensitive to the vertical miss distance and angle of attack. Hence, it is concluded that, setting aside the vortex–blade interaction effects, the blade–blade interaction may become an important factor in predicting the noise of the coaxial helicopter.

Effect of Viscosity

Most features of any flowfield can be captured by Euler equations, but viscosity may play an important role in some cases. Inviscid and viscous computations are performed for the same transonic flowfield and compared with each other to determine the viscosity effects on the flowfield. The flow condition is the same as in the preceding calculation. The histories of the lift and pitching moment fluctuation rate are shown in Fig. 11 for both inviscid and viscous cases. It is observed that qualitative behaviors show similar trends in both cases. However, the lift fluctuation rate of the upper airfoil is found to be weakened by 10–15% in the viscous computation, whereas the pitching moment is more sensitive to viscosity. In general, the viscosity has a tendency to attenuate the fluctuating intensity. For the lower airfoil, the inviscid result shows good agreement with the viscous one. It is concluded that viscosity has little effect on the overall characteristics but attenuates the fluctuating intensity. Hence, viscous effects can be neglected when the qualitative trend is of primary concern, as in the present study. The following computations are performed by solving Euler equations to reduce the computation time.

Effect of Vertical Miss Distance

Figure 12 shows the effects of the vertical miss distance on the load fluctuation while the angle of attack is kept constant at 10 deg. The measure of fluctuation decreases with the vertical miss distance as expected. As shown in Fig. 12b, the slope and the amplitude of the fluctuating force increase steeply with a decrease in the vertical miss distance. When $Y_{miss} = 1.5C$, ΔC_l reaches about 50% of the initial lift. The minimum lift occurs around $X_{miss} = 2.0C$ for all

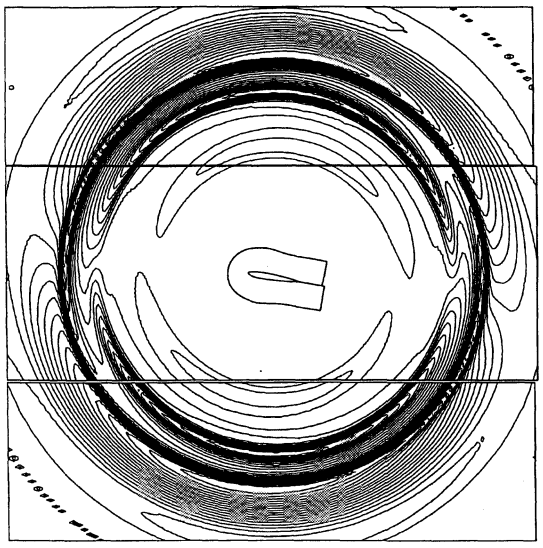

Fig. 10a Acoustic density around upper airfoil with respect to moving coordinates (M_l = 0.8, M_u = 0.8, α_l = 10 deg, α_u = 10 deg, X_{miss} = 7.5C, Y_{miss} = 1.0C, and $Re = 3 \times 10^6$).

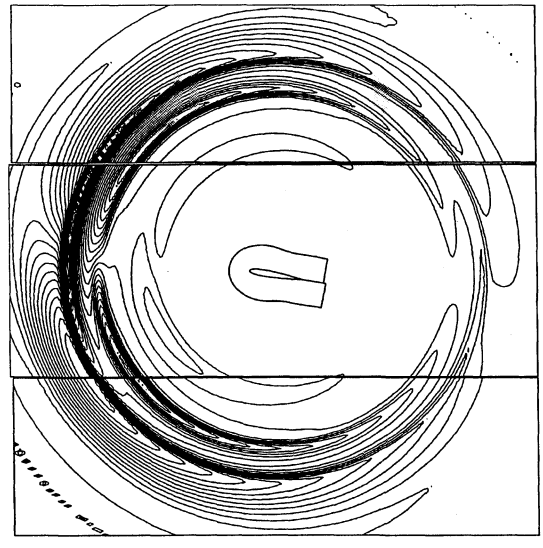

Fig. 10b Acoustic density around upper airfoil with respect to fixed coordinates (M_l = 0.8, M_u = 0.8, α_l = 10 deg, α_u = 10 deg, X_{miss} = 7.5C, Y_{miss} = 1.0C, and $Re = 3 \times 10^6$).

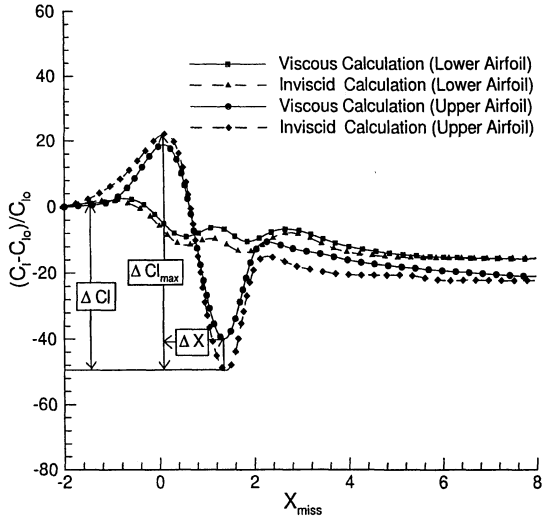

Fig. 11 Lift fluctuation rate of upper airfoil for viscous and inviscid cases (M_l = 0.8, M_u = 0.8, α_l = 3 deg, α_u = 3 deg, Y_{miss} = 1.0C, and $Re = 3 \times 10^6$).

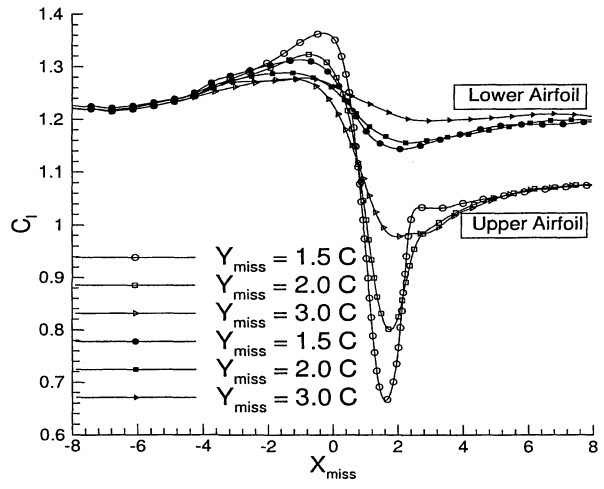

Fig. 12a C_l histories with a variation of Y_{miss} (M_l = 0.8, M_u = 0.8, α_l = 10 deg, and α_u = 10 deg, inviscid calculation).

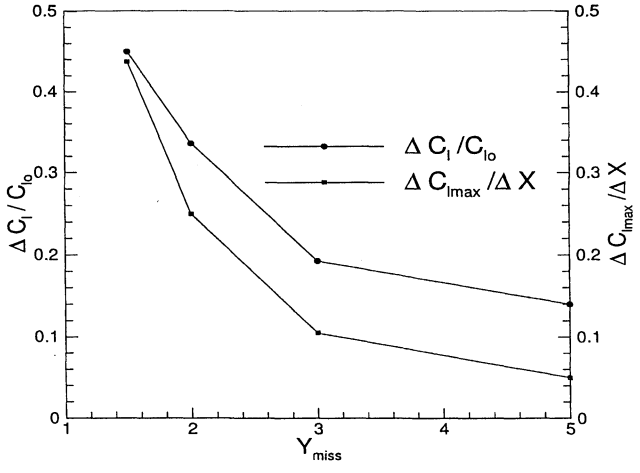

Fig. 12b $\Delta C_l/Cl_o$ and $\Delta Cl_{max}/\Delta X$ with a variation of Y_{miss} (M_l = 0.8, M_u = 0.8, α_l = 10 deg, α_u = 10 deg, inviscid calculation).

cases. It is noticeable that the lift history shows a similar behavior after $X_{miss} = 5.0C$ independent of the vertical miss distance, which implies that the vertical miss distance has its major effect on the fluctuation intensity and is not involved the overall flow characteristics. An overshoot of lift is observed from $X_{miss} = -4.0C$ slightly before the two airfoils meet. This intensity decreases with the vertical miss distance. On the other hand, the lower airfoil experiences only small changes with the vertical miss distance. Note that the vertical miss distance has no influence on the recovered lift level at the given angle of attack. That is, the vertical miss distance affects only the magnitude and the slope of the fluctuation.

Effect of Angle of Attack

A series of parametric studies was carried out with respect to the angle of attack of the lower airfoil varying from 2 to 10 deg with the upper airfoil angle of attack fixed, as shown in Fig. 13. The Mach number is 0.8, and the vertical miss distance is 1.5C. The overall behaviors are similar, but the recovered lift levels are different for all cases. This means hysteresis is directly related to the shock wave intensity of the lower airfoil. The minimum lift location shifts slightly in the positive X_{miss} direction as the lower airfoil's angle of attack increases. Consequently, the shock location of the lower airfoil also moves backward as the angle of attack increases. It is clear from Fig. 13b that the relation between ΔC_l and the lower airfoil's angle of attack is almost linear. It is also found that the lift history is different after $X_{miss} = 5.0C$ compared with Fig. 12. The recovery rate of lower lift varies with angle of attack.

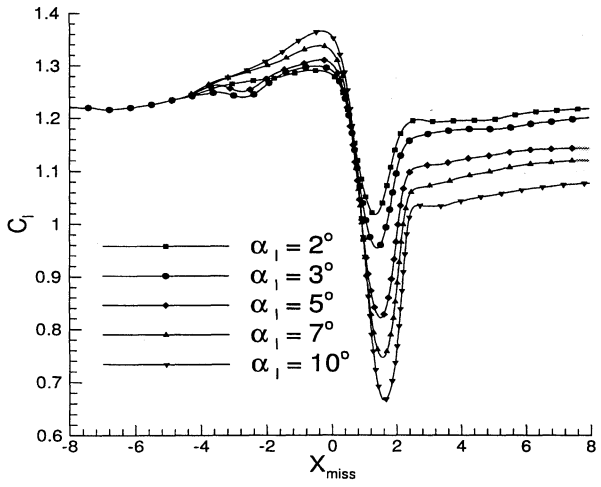

Fig. 13a C_l histories with a variation of α_l (M_l = 0.8, M_u = 0.8, α_u = fixed at 10 deg, and Y_{miss} = 1.5C, inviscid calculation).

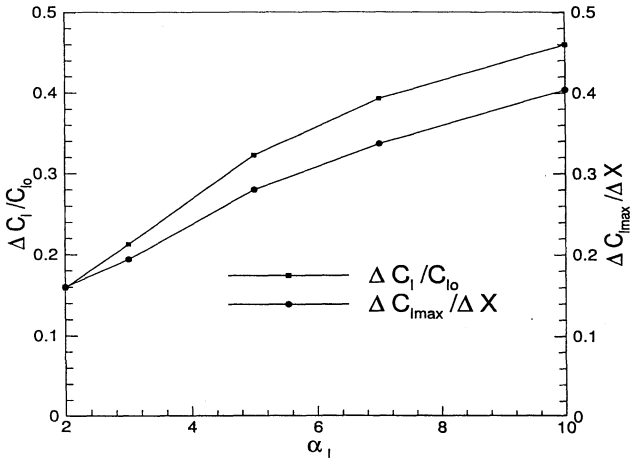

Fig. 13b $\Delta C_l/Cl_o$ and $\Delta Cl_{max}/\Delta X$ of upper airfoil with a variation of α_l (M_l = 0.8, M_u = 0.8, α_u = fixed at 10 deg, and Y_{miss} = 1.5C, inviscid calculation).

Concluding Remarks

The present study explores a transonic AAI. Ogawa and Fujii's[7] method is modified to give an appropriate initial condition for an asymmetric unsteady flowfield and proved to be efficient for saving overall computation time. Through a series of parametric computations, the following features are observed. 1) The upper airfoil undergoes severe aerodynamic load fluctuation during AAI resulting from the reduction of stagnation pressure and the rapid oscillation of the shock wave location. On the other hand, the fluctuation intensity of the lower airfoil is relatively small because lift loss is compensated by the retardation of the shock wave location. 2) Hysteresis is caused by the wake that modifies the ambient flowfield, and its influence continues long after the interaction. 3) A strong sound wave is radiated from the upper airfoil due to the pressure fluctuation near the leading edge (lift dipole dominant) right after the shock wave of the lower airfoil hits the stagnation region. 4) The intensity and the slope of the aerodynamic load fluctuation are more sensitive to the vertical miss distance than to the angle of attack. With a decrease in the vertical miss distance, the intensity of the load fluctuations increases steeply, whereas the variation of the angle of attack shows almost a linear increase.

Acknowledgment

This work was supported by the Korea Science and Engineering Foundation through the Turbo and Power Machinery Research Center at Seoul National University.

References

[1]Dougherty, F. C., "Development of a Chimera Grid Scheme with Applications to Unsteady Problems," Ph.D. Dissertation, Dept. of Aeronautics and Astronautics, Stanford Univ., Stanford, CA, June 1985.

[2]Kao, K.-H., and Liou, M.-S., "Advances in Overset Grid Schemes: From Chimera to DRAGON Grids," *AIAA Journal*, Vol. 33, No. 10, 1995, pp. 1809–1815.

[3]Steger, J. L., and Benek, J. A., "On the Use of Composite Grid Schemes in Computational Aerodynamics," *Computer Method in Applied Mechanics and Engineering*, Vol. 64, Oct. 1987, pp. 310–320.

[4]Dougherty, F. C., Benek, J. A., and Steger, J. L., "On Applications of Chimera Grid Schemes to Store Separation," NASA TM 88193, Oct. 1985.

[5]Kim, H. M., "Unsteady Flow Analysis of a Multi-Element Airfoil Using Overlapping Grid Scheme," M.S. Thesis, Dept. of Aerospace Engineering, Seoul National Univ., Seoul, Republic of Korea, Feb. 1995.

[6]Belk, D. M., "Unsteady Three-Dimensional Euler Equations Solutions on Dynamic Blocked Grids," Ph.D. Dissertation, Dept. of Aerospace Engineering, Mississippi State Univ., Mississippi State, MS, 1986.

[7]Ogawa, T., and Fujii, K., "Numerical Simulation of Compressible Flows Induced by a Train Moving Into a Tunnel," *Computational Fluid Dynamics Journal*, Vol. 3, No.1, 1994, pp. 63–84.

[8]Fujii, K., "Unified Zonal Method Based on the Fortified Solution Algorithm," Inst. of Space and Astronautical Science, Rept. 648, Japan, Dec. 1992.

[9]Coleman, C. P., "A Survey of Theoretical and Experimental Coaxial Rotor Aerodynamic Research," 19th European Rotorcraft Forum, Cernobbio, Italy, Sept. 1993, pp. D11.1–11.28.

[10]Nagashima, T., and Nakanishi, K., "Optimum Performance and Load Sharing of Coaxial Rotor in Hover," *Journal of Japan Society for Aeronautics and Space Sciences*, Vol. 26, No. 293, 1978, pp. 325–333.

[11]Saito, S., and Azuma, A., "A Numerical Approach to Coaxial Rotor Aerodynamics," *Proceedings of the 7th European Rotorcraft and Powered Lift Forum*, Vol. 24, Garmish-Partenkirchen, Germany, 1981 (Paper 42).

[12]Lee, S., "Strong Parallel Blade–Vortex Interaction and Noise Propagation in Helicopter Flight," Ph.D. Dissertation, Dept. of Aeronautics and Astronautics, Stanford Univ., Stanford, CA, 1992.

[13]Srinivasan, G. R., and McCrosky, W. J., "Aerodynamics of Two-Dimensional Blade–Vortex Interaction," *AIAA Journal*, Vol. 24, No. 10, 1986, pp. 1569–1576.

[14]Yee, K., Lee, D.-H., and Lee, S., "Numerical Analysis on the Flowfields Induced by Passing-by Airfoils with Transonic Speed," AIAA Paper 96-2512, June 1996.

[15]Roe, P. L., "Approximate Riemann Solvers, Parameter Vectors, and Difference Schemes," *Journal of Computational Physics*, Vol. 43, No. 3, 1981, pp. 357–372.

[16]Yee, H. C., Warming, R. F., and Harten, A., "Application of TVD Schemes for the Euler Equations of Gas Dynamics," *Lectures in Applied Mathematics*, Vol. 22, 1985, pp. 357–393.

[17]Sweby, P. K., "High Resolution TVD Schemes Using Flux Limiters," *Lectures in Applied Mathematics*, Vol. 22, 1985, pp. 289–309.

[18]Baldwin, B. S., and Lomax, J., "Thin Layer Approximation and Algebraic Model for Separated Turbulent Flows," AIAA Paper 78-0257, Jan. 1978.

[19]Pulliam, T. H., and Chaussee, D. S., "A Diagonal Form of an Implicit Approximate-Factorization Algorithm," *Journal of Computational Physics*, Vol. 39, No. 2, 1981, pp. 347–365.

[20]Rai, M. M., "A Conservative Treatment of Zonal Boundaries for Euler Equation Calculations," *Journal of Computational Physics*, Vol. 62, No. 2, 1986, pp. 472–503.

[21]Landon, R. H., "NACA0012 Oscillatory and Transient Pitching," AGARD R-702, Data Set 3, 1982.

[22]Mitchell, B. E., Lele, S. K., and Moin, P., "Direct Computation of the Sound from a Compressible Co-Rotating Vortex Pair," *Journal of Fluid Mechanics*, Vol. 285, 1995, pp. 181–202.

[23]Curle, N., "The Influence of Solid Boundaries upon Aerodynamic Sound," *Proceedings of the Royal Society of London, Series A: Mathematical and Physical Sciences*, Vol. 231, 1955, pp. 505–514.

S. Glegg
Associate Editor